

# Measurements of two-dimensional spatial coherence of normal-incidence seafloor scattering

Daniel C. Brown,<sup>1,a)</sup> Cale F. Brownstead,<sup>1</sup> Anthony P. Lyons,<sup>2</sup> and Thomas B. Gabrielson<sup>1</sup>

<sup>1</sup>The Applied Research Laboratory, The Pennsylvania State University, State College, Pennsylvania 16801, USA

<sup>2</sup>Center for Coastal and Ocean Mapping, University of New Hampshire, Durham, New Hampshire 03824, USA

(Received 15 April 2018; revised 10 September 2018; accepted 12 September 2018; published online 11 October 2018)

Measurements have been made near normal incidence of the two-dimensional spatial coherence of the acoustic field scattered from the lakebed in Seneca Lake, New York. In the test region, the lakebed consists of a series of sediment layers created by a sequence of distinct depositional processes. The spatial coherence length of the scattered field is shown to be dependent on the structure of the underlying sediment sequences. Significant ping-to-ping variability in the spatial coherence surface was also observed for each sediment sequence. This variability is quantified by a two-dimensional spatial coherence metric that measures the coherence lengths and asymmetric coherence surface orientation. The ping-to-ping variation of the surface asymmetry appears to be linked to the spatial isotropy of the sediment scattering strength. The scattering strength of the deepest observed sequence in the sub-bottom is the most spatially isotropic and the ping-to-ping variability of the coherence lengths and surface orientations are random. The scattering strength of the shallower sequences is spatially anisotropic and the coherence lengths and surface orientations show intervals of non-random ping-to-ping behavior. © 2018 Acoustical Society of America.

<https://doi.org/10.1121/1.5056168>

[BTH]

Pages: 2095–2108

## I. INTRODUCTION

The spatial coherence of the acoustic field scattered from the seafloor has been studied due to its importance in research areas such as array performance prediction and sediment property inversion. Typically, measurements are made of the total field scattered from the seafloor using either vertical or horizontal line arrays. In this work, measurements are made at normal incidence in a freshwater lake using a fully-populated two-dimensional horizontal receive array. This sensing geometry permits characterization of the horizontal two-dimensional spatial coherence of the scattered field.

A number of authors have described measurements of the spatial coherence of the field scattered from the seafloor (Berkson *et al.*, 1980; Berkson, 1980; Clay, 1966; Guillon *et al.*, 2011; Urlick and Lund, 1964). Early work by Urlick and Lund (1964) characterized the vertical coherence of scattering from the sea surface, deep scattering layer, and the seafloor. Clay (1966), Berkson (1980), and Berkson *et al.* (1980) used measurements of the spatial coherence of bottom scattering as a function of grazing angle to invert for the root-mean-square (rms) roughness of the seafloor. This inversion was accomplished by linking the measured frequency dependent spatial coherence to the frequency dependence predicted by Eckart's coherent reflection coefficient (Eckart, 1953). In Guillon *et al.* (2011), a complex layered seabed was shown to produce a nonlinear cross-spectral

phase for vertically separated hydrophones, and this nonlinearity is equivalent to a reduction in the spatial coherence of the measured field.

In addition to these measurements of the spatial coherence, several studies have focused on modeling the spatial coherence of the incoherent component of the scattered field. Jackson and Moravan (1984) extended the sea-surface scattering work of Frazier (1974), Wilson (1982), and Wilson and Frazier (1983), utilizing a point scattering model to study the horizontal spatial coherence of the scattered field. Smith and Atkins (1991) developed a model for the horizontal coherence for normal-incidence bottom-interface reverberation using the high-frequency Kirchhoff approximation for interface scattering. Finally, Tang and Frisk (1995) provided a model for investigation of the spatial coherence of plane wave scattering from inhomogeneities within the seafloor for frequencies spanning 40–200 Hz. Their model is the most realistic in terms of the physical description of the seafloor. It includes a variable thickness sediment layer with a small random sound speed component overlaying a half-space with no random sound speed component.

The present work describes experimental measurements of the two-dimensional spatial coherence of the field scattered near normal incidence at Seneca Lake. The study is motivated by several potential applications. Tang and Frisk (1995) hypothesize that spatial coherence measurements may be inverted to infer some geoaoustic sediment parameters. This assertion is supported in recent work by Brown (2017), where the van Cittert-Zernike theorem was used to model the spatial coherence of near-normal incidence sea

<sup>a)</sup>Electronic mail: dan.brown@psu.edu

floor scattering. It was shown that under some circumstances the spatial coherence was sensitive to the geoacoustic parameters of the sea floor. Another pair of potential applications are related to sensor motion estimation. First, the displaced phase center antenna motion estimation technique used by synthetic aperture sonar (SAS) systems exploits the spatial coherence of sea floor reverberation (Bellettini and Pinto, 2002). Application of this motion estimation technique to a normal-incidence SAS such as that described by Schock *et al.* (2001) would require an understanding of the spatial coherence of the field at normal incidence. Second, the correlation velocity log (CVL) is another type of motion estimation sensor that exploits spatial coherence near normal incidence. CVLs were originally described by Dickey and Edward (1978), and the error model proposed in their original work showed the sensor's accuracy is proportional to the scattered field's spatial coherence length. A final motivation for the present study is the area of array gain modeling. Arrays of acoustic receivers are frequently used to improve the detection of a signal against a background of ambient noise or reverberation. In the classic treatment, the gain of the receive array against isotropic, ambient noise is given by the directivity index (DI) or array gain (AG). In practice, the noise field may not always be idealized in this way. Experimental observations of the coherence lengths observed for reverberation in both deep water and shallow water waveguides are provided by Carey (1998). Carey's experimental observations of the coherence length led to the description of a "Carey Number," the wavelength normalized coherence length of the field (Lynch *et al.*, 2013). Thus, accurate descriptions for the coherence length of the seafloor scattered field may have application in the prediction of array gain available for a given environment.

Below, a general description of the sonar and data acquisition system are provided in Sec. II and the signal processing applied to the recorded data is reviewed in Sec. III. The test site and its geologic setting are described in Sec. IV. Finally, experimental results are described in Sec. V.

## II. SONAR SYSTEM

The sonar system utilized in this study consists of a 48 channel receive array and a single channel projector mounted to a nine meter pontoon boat. A photo of the boat and sonar is provided in Fig. 1. The sonar projector and receive array are seen mounted in a rectangular frame with several yellow cables in the forward portion of the boat. The projector, which is mounted in the aft portion of the sonar frame, has a circular face that is 53 cm in diameter. The receive array consists of six receiver modules with eight channels per module. The 48 receive array hydrophones are arranged in a rectangular 6-channel by 8-channel grid with a 9.14 cm center-to-center spacing. The array is positioned in the sonar frame with the 8-channel dimension in the fore-aft direction.

The sonar system was calibrated at the Acoustic Test Facility at the Applied Research Laboratory at The Pennsylvania State University. Beam patterns were measured for the projector and all 48 receive hydrophones. These beam patterns were measured from 16 to 20 kHz and a



FIG. 1. (Color online) The test platform for data collection is a 9 meter pontoon boat. The projector and receive array are shown mounted in the forward portion of the boat. These components are attached to a rectangular frame that is lowered into the water during testing.

band-averaged  $-3$  dB beamwidth was calculated from these beam patterns. The projector's beamwidth is 9 degrees and each receiver's beamwidth is approximately 60 degrees. The individual elements of the receive array are connected to an analog signal conditioning preamplifier prior to digitization. This preamplifier circuit provides 20 dB of gain, a single pole high-pass filter at 2 kHz, and an eight pole low-pass filter at 80 kHz. The signals are digitized by simultaneously sampled analog-to-digital converters operating at a sample rate of 200 kHz. During testing, the transmit source level is 215 dB re  $\mu$ Pa at 1 m. The transmit waveform for both tracks is a 10 ms linearly-frequency-modulated waveform from 12 kHz to 24 kHz. This waveform is windowed with a 10% Tukey window (Harris, 1978).

## III. SIGNAL PROCESSING

The sonar system described in Sec. II was used to collect normal incidence bottom reverberation while the test platform transited a series of nearly linear tracks over the deep central portion of the lake. Along each track, the sonar system transmitted flights which consisted of a pair of pulses separated by 100 ms at an inter-flight interval of  $\sim 850$  ms. The work presented here focuses on analysis of the first pulse in each flight.

The signals recorded for each flight were processed using the sequential series of steps shown in Fig. 2. The recorded data was replica correlated using an analytic replica of the transmit waveform. An example of a flight's signal after replica correlation is shown in Fig. 3. The direct-path signal from the transmitter to the receiver is seen at 10 ms and 110 ms, and the bottom returns are seen at 260 ms and 360 ms. The returns from the lake floor fall back to the background level approximately 80 ms after scattering. An additional weaker return is seen at 510 ms. This is the signal which scatters from the lake floor, is then reflected by the lake surface, scatters from the lake floor a second time, and is then received by the hydrophone.

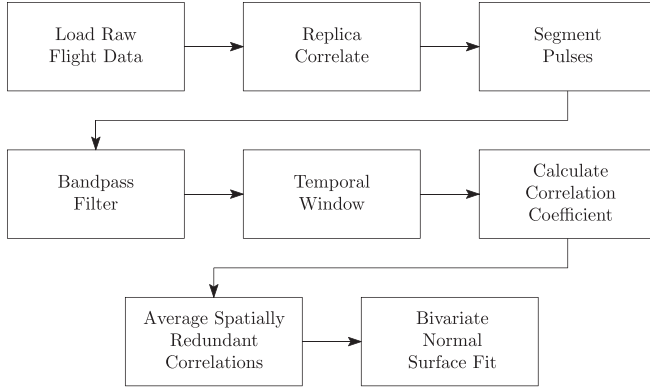


FIG. 2. The spatial coherence of the field data is measured and characterized through the sequence of signal processing steps shown here.

The signal of interest is the return from the lake floor at 260 ms. Beginning at this arrival time, a 100 ms record is extracted or segmented for each of the 48 receive array channels. A 16–20 kHz bandpass filter is then applied to the segmented pulses. An additional temporal window is then applied to isolate returns from specific sediment depths. After segmentation, filtering, and temporal windowing, the coherence between the channel pairs is estimated.

At this point, it is worth providing specificity in the definition “coherence” since there are two common technical uses of the term. The first use deals with characterization of the spectral similarity of a pair of signals. This measure is formally known as the coherence function, or magnitude-squared coherence, and it is given by the normalized cross-spectral density of a signal pair. This paper utilizes the second common usage of this term. In this definition, coherence refers to a measure of the temporal similarity of two signals. [Born and Wolf \(1999\)](#) describe the coherence as the similarity of the “fluctuations” of the observed field. For a pair of real, zero-mean signals  $s_1(t)$  and  $s_2(t)$  the population covariance at a lag or delay of  $\tau$  is defined as

$$\Gamma_{ij}(\tau) = \langle s_i(t)s_j(t+\tau) \rangle = \int s_i(t)s_j(t+\tau)dt. \quad (1)$$

The calculation of the population covariance requires an infinite temporal interval. In practice, a finite length signal is used to form an estimate of the population covariance. This finite length estimate is called the sample covariance. For a signal of length  $T$ , it is

$$\hat{\Gamma}_{ij}(\tau) = \begin{cases} \frac{1}{T} \int_{-(T-|\tau|)/2}^{(T-|\tau|)/2} s_i(t)s_j(t+\tau)dt, & 0 \leq \tau \leq T \\ 0, & |\tau| > T. \end{cases} \quad (2)$$

Evaluation of the sample covariance at zero-lag gives

$$\hat{\gamma}_{ij} = \hat{\Gamma}_{ij}(\tau = 0) = \langle s_i s_j \rangle = \frac{1}{T} \int_{-T/2}^{T/2} s_i(t)s_j(t)dt. \quad (3)$$

Normalization of the cross-covariance by the product of the component signal auto-covariances gives the sample correlation coefficient

$$\hat{\mu}_{12} = \frac{\hat{\gamma}_{12}}{\sqrt{\hat{\gamma}_{11}\hat{\gamma}_{22}}}. \quad (4)$$

It is this sample correlation coefficient that is used throughout this paper as an estimate of the coherence between a pair of signals. The zero-lag correlation coefficient is used as opposed to the peak of the cross correlation because the latter is biased for weakly correlated signals. Since this data was collected on a lake, the collection platform was relatively stable. If the data collections had been made in a less benign environment, then platform motion effects would have to have been taken into account.

The channel-to-channel correlation of a pulse produces  $48^2$  measures of the correlation coefficient. Each of these measures has an associated spatial offset; however, the offsets are not unique. For example, the autocorrelation produces 48 measurements of correlation coefficient at zero spatial offset. A regularly spaced rectangular array with dimensions  $m \times n$  has  $(mn)^2$  correlation pairs with  $(2m-1)(2n-1)$  unique spatial offset positions. Thus, the  $6 \times 8$  channel receive array used in this experiment produces an  $11 \times 15$  array of unique spatial offsets.

At any unique spatial offset, the redundant correlations are averaged to form the  $11 \times 15$  matrix of correlation coefficients. This same approach to averaging the redundant correlations has been discussed by [Boltryk et al. \(2004\)](#) in the context of the signal processing for correlation velocity log sonar systems. The  $11 \times 15$  matrix of correlation coefficients is shown for ping 300 of track 192 329 in Fig. 4. In this figure, the  $x_1$  axis represents port-starboard displacement and the  $x_2$  axis represents fore-aft displacement. This spatial representation of the data greatly aids interpretation of the measured correlation coefficients. The two-dimensional spatial coherence surface is a maximum at zero displacement and falls monotonically near the peak. Note that the surface does not exhibit radial symmetry and instead has two principal axes of symmetry that are not aligned to the array coordinates.

The coherence lengths and orientation of the two-dimensional surface in Fig. 4 are quantified using the “bivariate normal surface fit” metric proposed by [Brown et al. \(2017\)](#). This metric fits a function similar to a bivariate Gaussian to characterize the coherence lengths and surface asymmetry. The form of the basis function is

$$\mu = \mu_p \exp \{ -\mathbf{x}^T \Sigma^{-1} \mathbf{x} \}, \quad (5)$$

where  $\mathbf{x} = [x_1 \ x_2]^T$  and

$$\Sigma = \begin{bmatrix} \sigma_1^2 & \rho\sigma_1\sigma_2 \\ \rho\sigma_1\sigma_2 & \sigma_2^2 \end{bmatrix}. \quad (6)$$

$\sigma_1$  and  $\sigma_2$  are the widths of the spatial coherence along the respective axes defined by the array coordinates,  $\rho$  provides a measure of asymmetry and surface orientation, and  $\mu_p$  is the peak of the function fit to the measured correlation coefficients. Coherence lengths aligned to the major and minor axes of the asymmetric surface are found through an eigen-decomposition of the covariance matrix, Eq. (6). The eigen-decomposition produces  $\sigma_a$ , the major axis coherence length;



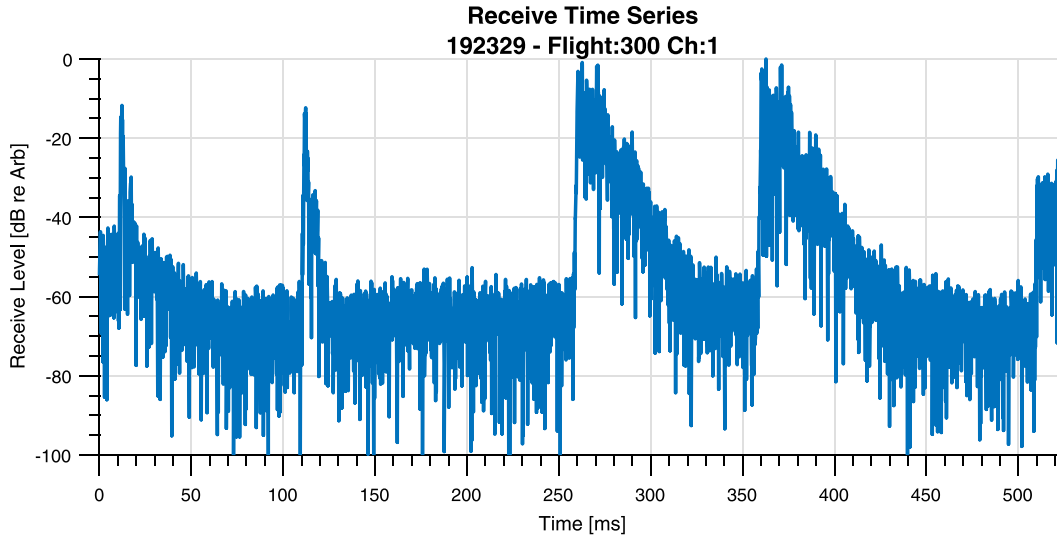


FIG. 3. (Color online) The full time series for flight 300 is shown for track 192 329. The two initial returns are direct-path from the transmitter to the hydrophone. The bottom returns arrive at 260 ms and 360 ms. The later return at 510 ms is the signal which scatters from the lake floor, is then reflected by the lake surface, and scatters from the lake floor a second time prior to reception.

$\sigma_b$ , the minor axis coherence length; and  $\theta_a$ , the orientation of these axes.  $\theta_a$  is defined so that  $\theta_a = 0$  indicates that the major axis is aligned with the  $x_1$  axis. Therefore, if  $\theta_a = 0$  then  $\sigma_a = \sigma_1$  and  $\sigma_b = \sigma_2$ . Using the coherence lengths aligned to the major and minor axes it is possible to define a single measure of the surface asymmetry,  $\varepsilon = \sigma_b / \sigma_a$ . This measure of asymmetry is bounded such that  $\varepsilon \in (0, 1]$ .  $\varepsilon = 1$  is the case of no asymmetry (a circular surface) and the most extreme asymmetry occurs as  $\varepsilon \rightarrow 0$ . The surface fit has been applied to the measured data in Fig. 4 and the resulting fit parameters are given in the figure's title. The coherence length is 42 cm along the main axis and 23 cm along the minor axis. The resulting asymmetry factor is  $\varepsilon = 0.56$ , and the surface is oriented with  $\theta_a = -36.9$  degrees. The measurement geometry for the data shown here is axisymmetric, yet the surface shows significant asymmetry. This

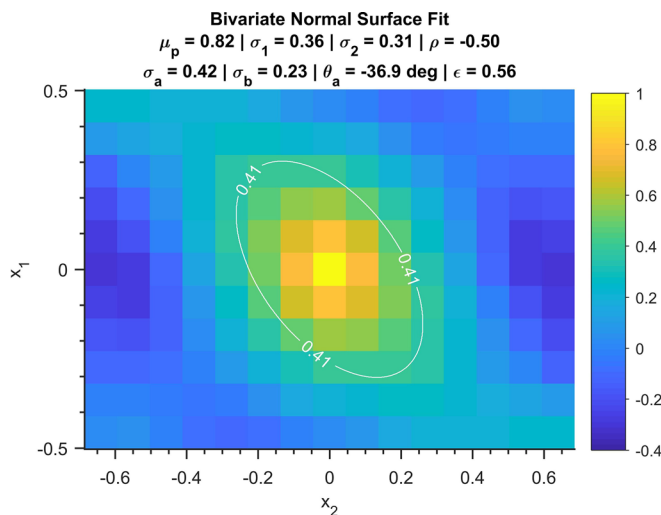


FIG. 4. (Color online) The two-dimensional spatial coherence is calculated for ping 300 of track 192 328. This surface was calculated using a 10 ms temporal window starting 35 ms after the initial bottom return. The shape of this surface is characterized using the bivariate normal surface fit, and the definitions of these parameters are provided in Sec. III.

asymmetry may be due to small collections of natural inhomogeneous material or the presence of slight tilts in the lake floor structure. Brown *et al.* (2017) has proposed a spatial coherence model that shows seafloor slope can lead to asymmetric spatial coherence. Those modeling results indicated significant asymmetry required slopes in excess of 5 degrees, which is much greater than any found in the test site.

#### IV. SENECA LAKE TEST SITE

The experimental data presented here was collected at Seneca Lake, New York, which is one of eleven lakes located in an area of New York state known as the Finger Lakes region. Seneca Lake is the largest by volume of these lakes with a 186 m maximum depth, a 57 km length, and a 5 km width at its widest point (Halfman, 2011). A bathymetric map of the lake, provided by Mullins *et al.* (1996), is shown in Fig. 5. Acoustic testing was conducted near Squaw Point along a set of nominally straight tracks in the central portion of the lake in 180 meters of water. The two collections studied are “2015 0615 182908” and “2015 0618 192 329,” where the track identification is given by the date and UTC time of the track's initial transmission. The remainder of this paper will distinguish the two collections using the final six digits of the track identifier.

A profile of the acoustic returns has been formed from 200 sequential transmissions over the first 200 m of track 192 329. The initial bottom return is used to temporally align these signals prior to incoherent averaging. The average return, normalized to the maximum level, is shown in Fig. 6. Three sediment sequences are identified in this figure. Sequence 3 corresponds to the uppermost interval, and the field scattered from this sequence is characterized by an initially high specular response. Following this initial return, the level decreases by roughly 10 dB and is variable with clear vertical (depth) structure. The mean level of the field scattered from sequence 2 is approximately 20 dB lower than the mean level of sequence 3. This scattered level varies

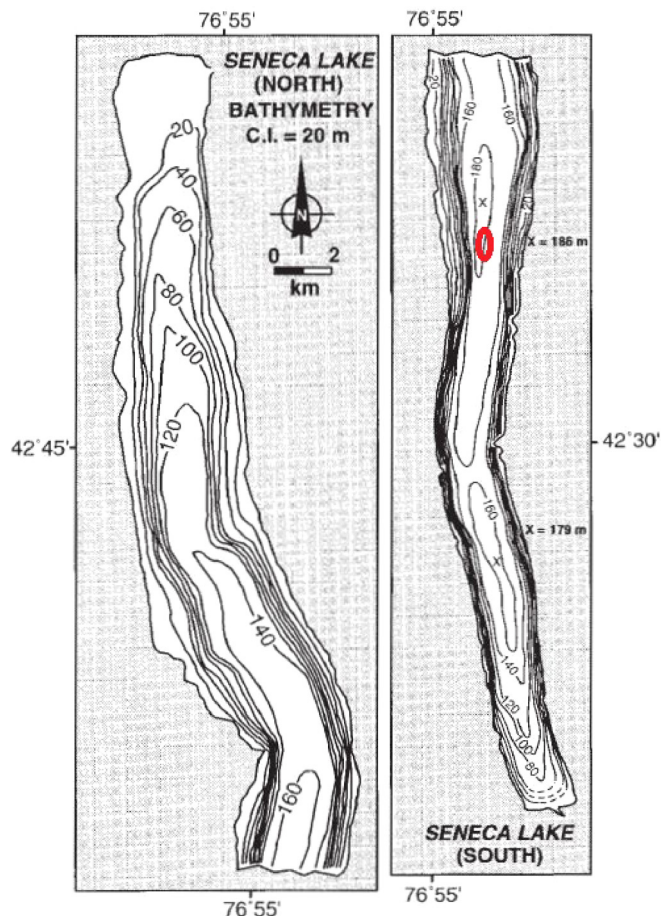


FIG. 5. (Color online) Seneca Lake is located in New York's Finger Lakes Region and it is the largest by volume of the eleven lakes in this area. The central portion of Seneca Lake has a deep and flat lake floor at more than 140 m depth. The test site is called out with a red oval. Figure from Mullins *et al.* (1996).

little with depth and it exhibits significantly less vertical structure than that found in sequence 3. The level of the field scattered from the sequence 1 sediments, which lie beneath sequence 2, fall with depth. Additionally, these returns show no depth structure except for a small enhancement near 220 meters depth.

The sonar data for track 192 329 has been processed to produce a sub-bottom profile showing the lake bathymetry and sub-bottom sediment structure (see Fig. 7). This track was collected on a roughly north-to-south heading, and the lakebed slope in this direction is less than 0.5 degrees. This sub-bottom profile is reproduced in Fig. 8, where the depth axis and dynamic range of the display are truncated to emphasize the spatial variability of the scattering in the sequence 2 sediments. Additional data collected in this portion of the lake shows the east-to-west slope is less than one degree. It will be shown that the structure associated with each sequence in Fig. 6 has a strong impact on the measured two-dimensional spatial coherence.

The specific sediment structures observed in these sub-bottom profiles are best interpreted after reviewing the processes responsible for sediment deposition on the lakebed. The Finger Lakes were formed through a sequential glacial erosion and sediment infilling process during the Holocene period more than 14 000 years ago (Coates, 1968; Mullins and Hinchey, 1989). The bedrock beneath the glacial ice sheet was eroded due to large scale glacial drainage. This erosion process produced a deep V shaped trough in the bedrock. Following the erosion, sediment transport during deglaciation infilled the lake creating an east-to-west profile with steep sides and a flat lake bed. This bathymetric profile has been observed in a number of seismic surveys (Halfman and Herrick, 1998; Lyons and Weber, 2007; Mullins and Hinchey, 1989; Mullins *et al.*, 1996; Weber and Lyons, 2006) and can be seen in Fig. 5.

The two principal studies of the Seneca Lake bed sediment stratigraphy have been conducted by Mullins *et al.* (1996) and Halfman and Herrick (1998). Each author described a series of sedimentation processes responsible for the depositional sequences making up the lake floor. Here, the six sequences described by Mullins *et al.* (1996) are notated M1–M6 and the four sequences of Halfman and Herrick (1998) are notated HH1–HH4. Note that it is customary to number the sequences in ascending depth order so that the uppermost sequence has the highest number.

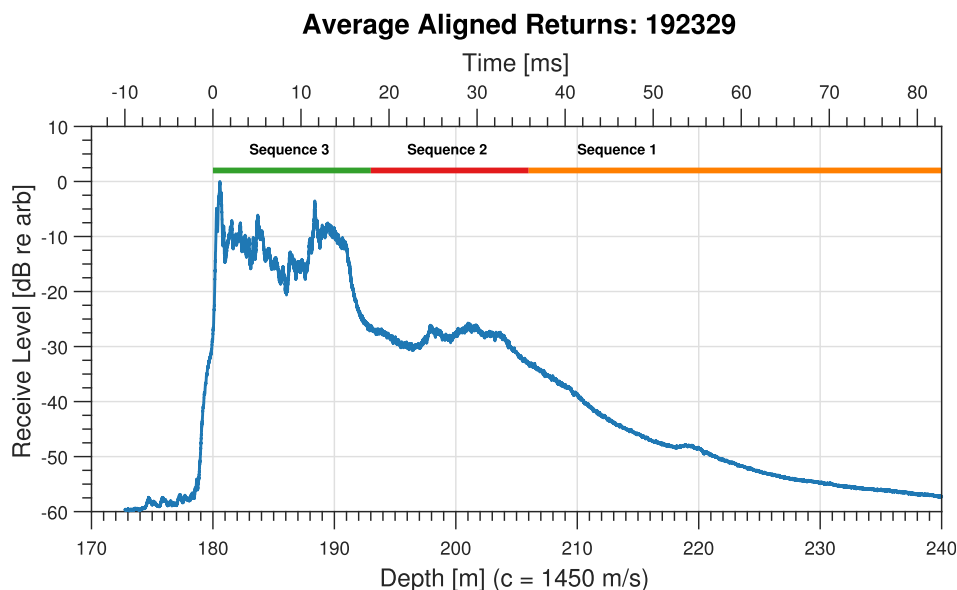


FIG. 6. (Color online) An averaged return from track 192 329 is shown as a function of depth from the sensor and time after the first interface return. Three distinct sediment sequences are identified. This plot is created by incoherent averaging of the first 200 pings of Track 192 329.



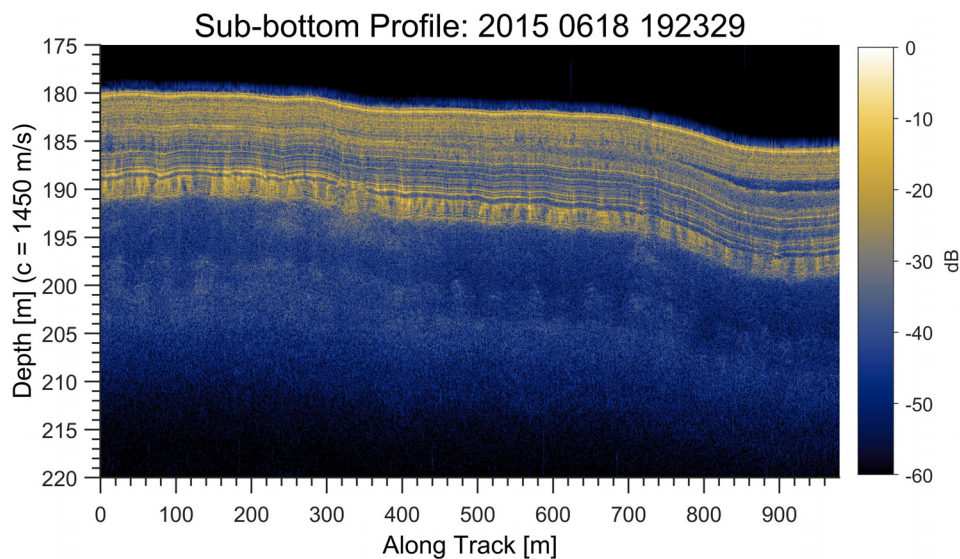


FIG. 7. (Color online) This sub-bottom profile of the lake bed was collected on a North-to-South track near Squaw Point in the center of the lake. This sub-bottom profile was created using a 10 ms 12–24 kHz linearly frequency modulated waveform and replica correlation. The temporal sidelobes of the ambiguity function are seen as a thin margin of return leading the main interface return.

Using this pair of prior studies, it is possible to provide some interpretation of Figs. 6–8. The upper 10–12 meters show enhanced acoustic scattering and a horizontal layered structure. This sequence is identified in the stratigraphic studies as HH4 or M6. Both studies describe the uppermost sequence as a “laminated black mud” that was created through post-glacial depositional process. The studies indicate that the sequence’s thickness is a maximum in the deep central portion of the lake where the present study was conducted. Both Mullins *et al.* (1996) and Halfman and Herrick (1998) noted the sediment thickness was measured to be greater than 5 meters in this portion of the lake.

Curtin *et al.* (2008) has hypothesized that the layering observed in this portion of the lake is due to sediment transport associated with large scale rain events. Ludlam (1967) has studied sediment transport processes for nearby Cayuga Lake, and he found basin-wide laminae that he associated with regional flooding events. The major layers, found in Cayuga, were frequently separated by more than 10 cm. It is likely that these major layers are the source of scattering for the interfaces observed in Fig. 7.

Sequence 2 lies beneath sequence 3, and the character of this sequence’s scattered returns is markedly different. Distinct layering is not present and the scattering level is weaker and spatially irregular. The lower boundary of sequence 2 consists of a weak and diffuse interface approximately 10–12 meters below the upper sequence boundary. The spatial irregularity of the scattering from this sequence is clearly seen in Fig. 8, where the depth axis and dynamic range are truncated. The challenge is to associate the acoustic character of the sediments observed at these depths with the prior geologic interpretation. Mullins *et al.* (1996) described both M4 and M5 as a series of highly-reflective layers whose composition was either clay or mud. The character of sequence 2 observed in the sub-bottom profiles collected in this experiment are not well described by Mullins *et al.* Halfman and Herrick (1998) described HH3 as a pair of mass-movement deposits that produced a near-transparent and irregular acoustic return. HH3 deposits were found to be up to 10 meters thick. This agrees well with the observations in the data; however, Halfman and Herrick noted that HH3 thinned moving southward in their study area. HH3 was

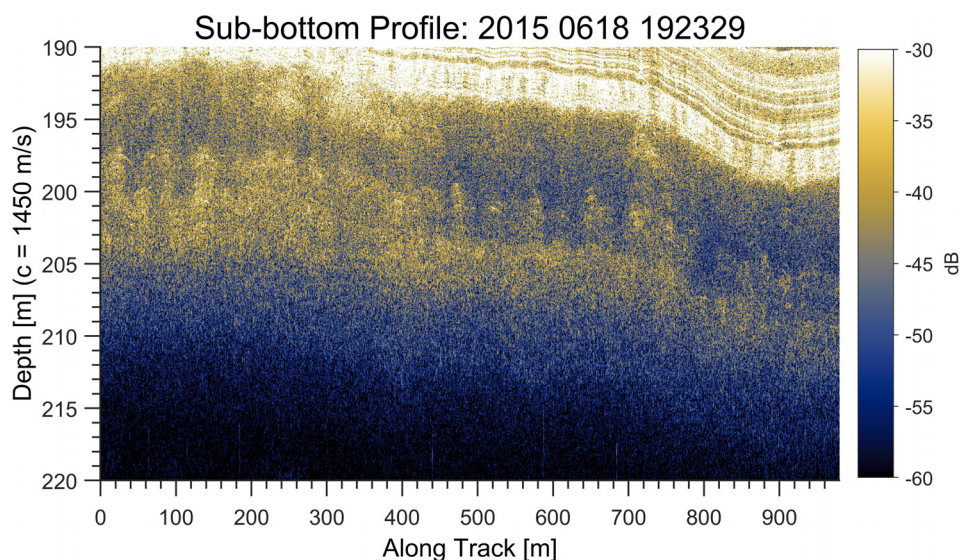


FIG. 8. (Color online) The sub-bottom profile of Fig. 7 is shown zoomed in on the portion of the return beneath the uppermost layered interface. The dynamic range has been scaled to emphasize the spatial anisotropy of the returns.

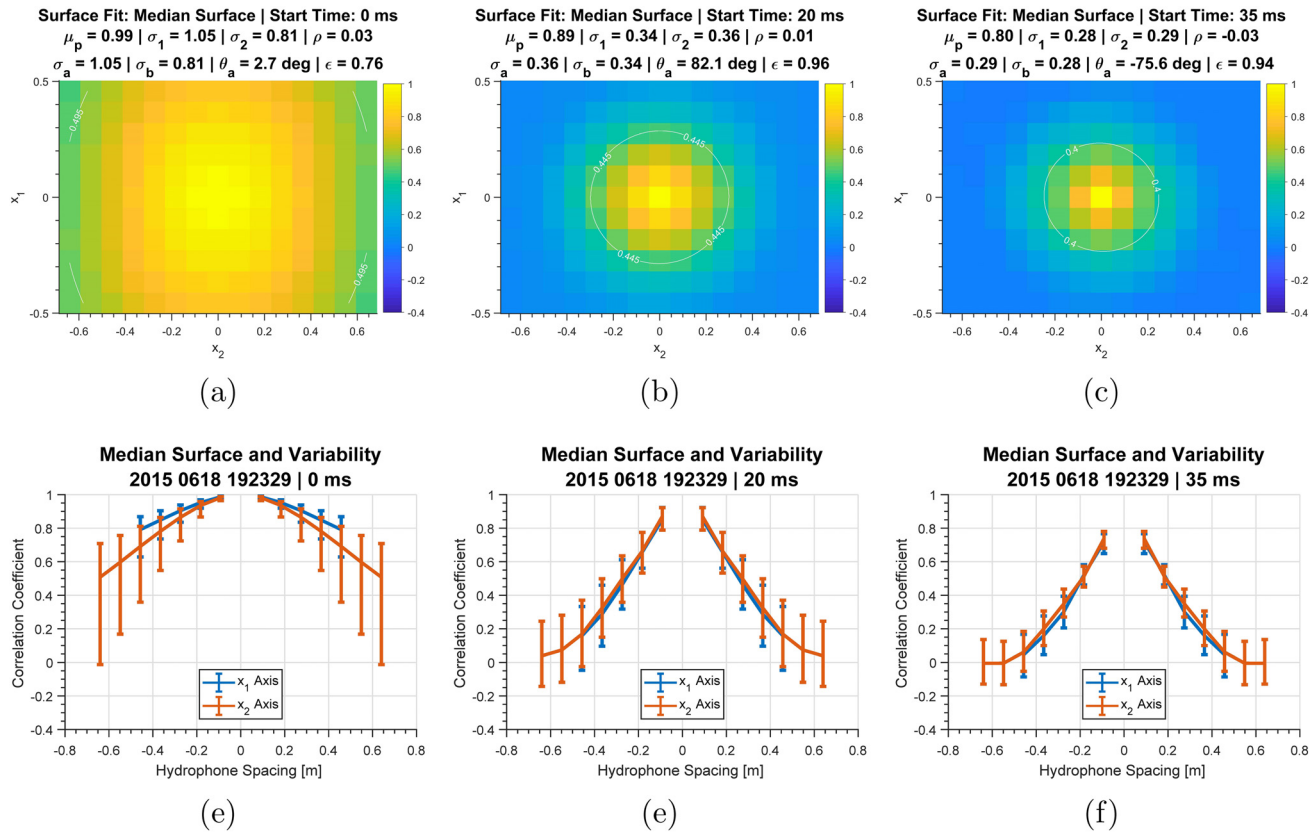


FIG. 9. (Color online) The median spatial coherence surface has been calculated for 1000 ping ensemble of surfaces for track 192 329. The median surface is shown in the upper row for the 0 ms, 20 ms, and 35 ms temporal windows in the left, center, and right columns rows, respectively. These windows were selected to correspond to the three sediment sequences identified in Fig. 6. The lower row provides a fore/aft and port/starboard slice through each of the median surfaces with error bars indicating the 80% measurement interval.

absent south of Dresden, NY. The data for the present study was collected 10 km south of the southernmost point of the Halfman and Herrick study. Halfman and Herrick described HH2, which is overlaid by HH4 in the absence of HH3, as a

highly reflective series of layers, which does not agree with the character of the data. It may be possible that the sequence 2 sediment observed in the present study's data is similar to HH3 but is associated with a separate mass

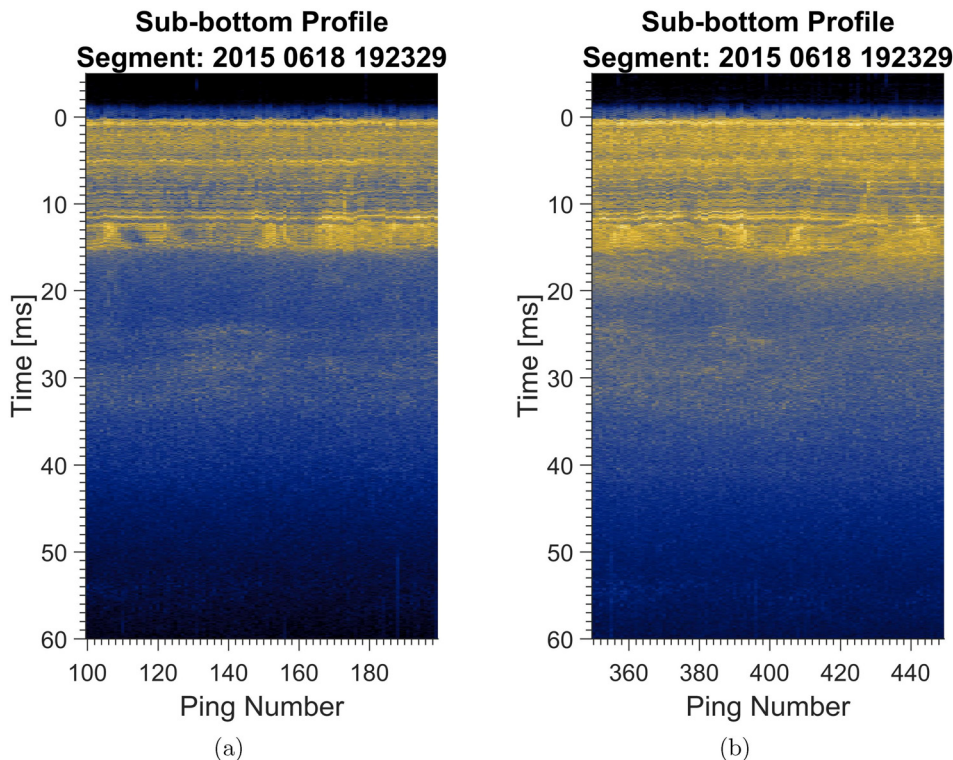


FIG. 10. (Color online) Sub-bottom profiles are shown in the area of pings 155 and 408 for track 192 329. Qualitatively the sub-bottom profiles are similar for this pair of pings.



movement event from that observed in the Halfman and Herrick study.

Profiles of the water temperature versus depth were also collected in the lake during the test period. The water temperature was 16°C near the surface and falling to 4°C by a depth of 50 m. Below this depth, the lake was isothermal with a constant sound speed near 1423 m/s. The mean sediment sound speed was estimated to be 1458 m/s in a separate experiment using the same data collection platform and a pair of hydrophones moored in the water column. The sound speed inversion technique employed was first described by Bryan (1980) and involves inversion of the range migration of sub-bottom wavefronts as a function of ensonification angle for the bulk sound speed in the sediment.

## V. RESULTS AND DISCUSSION

The sonar system and signal processing described in the prior sections was used to collect and analyze data at Seneca Lake, NY. The signal processing approach discussed in Sec. III described a temporal windowing step for isolating the sub-bottom returns from specific sediment sequences. In the results presented in this section, nine distinct temporal windows are utilized. Each of the nine windows are 10 ms in length and they vary in their starting or inner time in 5 ms intervals. The first window's inner time is 0 ms, and this corresponds to the window encompassing the first 10 ms of the return from the bottom. The second window spans 5–15 ms and the remainder of the windows proceed in this fashion with the inner time incrementing in 5 ms steps.

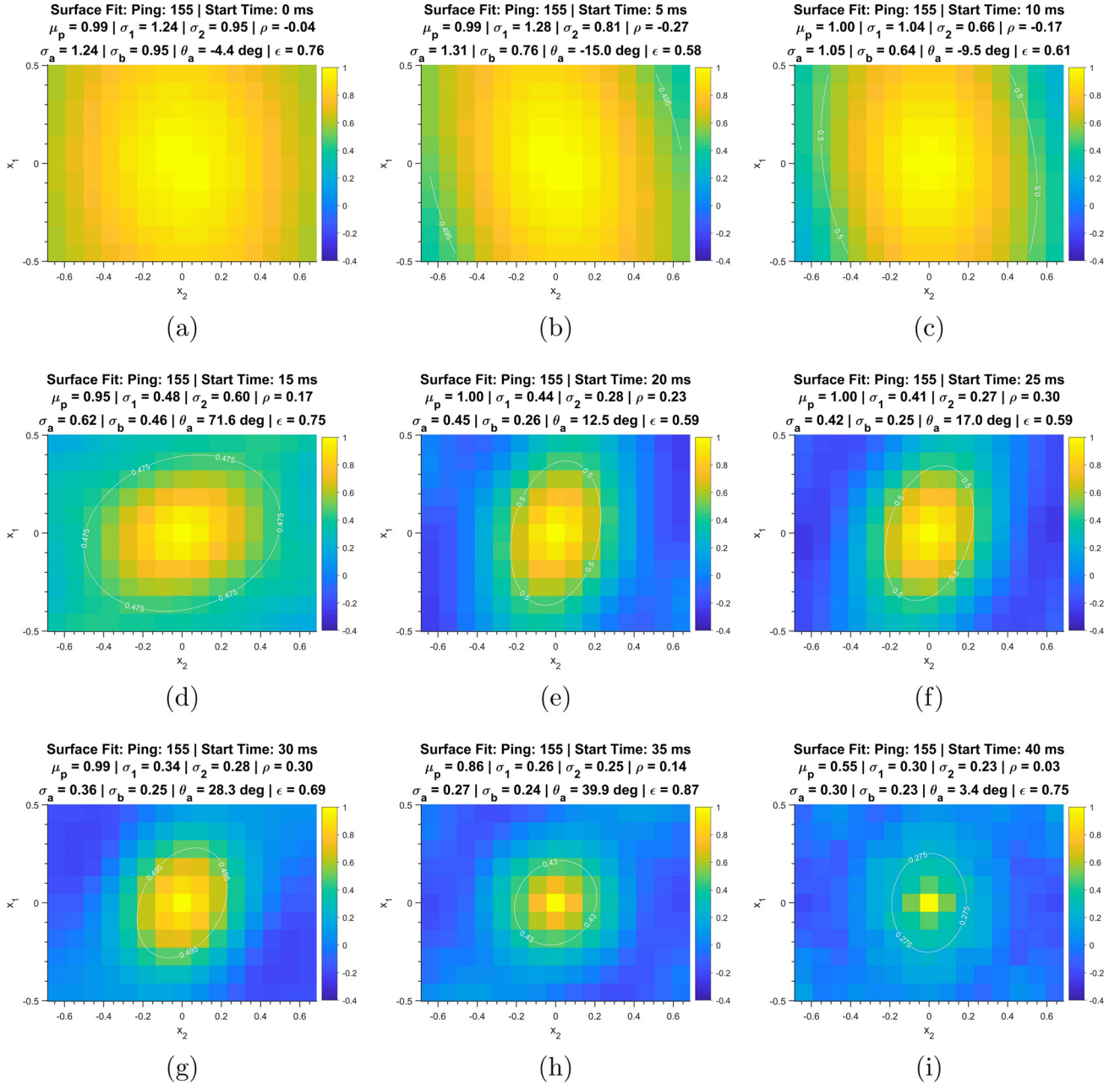


FIG. 11. (Color online) The spatial coherence surface is shown for nine different temporal windows applied to ping 155 of track 192 329. Each figure was created with a 10 ms temporal window. The starting or inner time, which is shown in the figure title, is incremented in 5 ms steps from the onset of the initial bottom return. The shape of each surface is measured using the bivariate normal fit and the fit parameters are also provided in the figure title.



Track 192 326 consists of 1000 sequential pings, and the inter-ping displacement of the sonar is approximately 1 meter. The spatial coherence surface was calculated for each of the 1000 pings and for each of the nine temporal windows described above. In Fig. 9, the median spatial coherence surface, calculated across the 1000 ping ensemble, is shown in the upper row for the temporal windows with inner times of 0 ms, 20 ms, and 35 ms. These three inner times were selected so that they correspond to the three sediment sequences described in Fig. 6. The lower row shows the fore/aft and port/starboard slices through this median surface with error bars indicating the 80% measurement interval. The median and 80% interval were selected over statistical moments for characterizing the coherence measurements due to the skewed distribution of correlation coefficient for

highly correlated fields (Stewart and Ord, 1994). The sequence 3 window shows moderate surface asymmetry as well as significant variance in the measured correlations. Sequence 2 and sequence 1 each show a median surface with little asymmetry, decreased coherence length, and reduced variance in the measured correlation coefficient.

A pair of pings (155 and 408) have been selected from track 192 329 for more detailed analysis. This pair of pings are separated by approximately 250 meters (Note: at these frequencies and ranges the first Fresnel zone has a diameter of 5.4 meters). Segments of the sub-bottom profile centered on the selected pings are shown in Fig. 10. Qualitatively, there are no obvious differences between these profiles. Each sub-bottom segment shows sequence 3 dominated by highly-reflective, post-glacial, layered sediments. Distinct

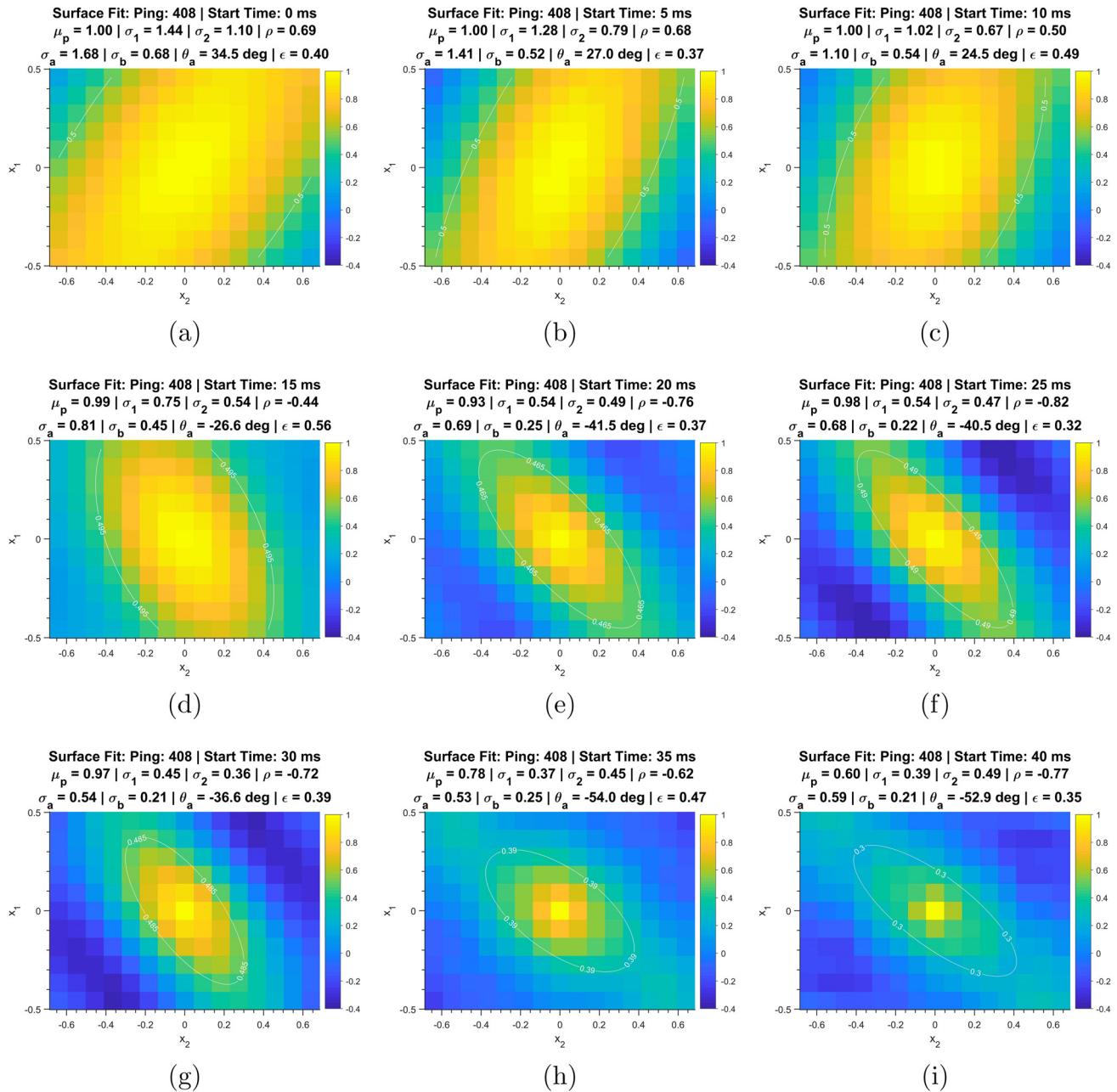


FIG. 12. (Color online) The spatial coherence surface is shown for ping 408 of track 192 329 using the same temporal windows applied in Fig. 11. The shape of each surface is measured using the bivariate normal fit and the fit parameters and inner time are provided in the title of each figure.

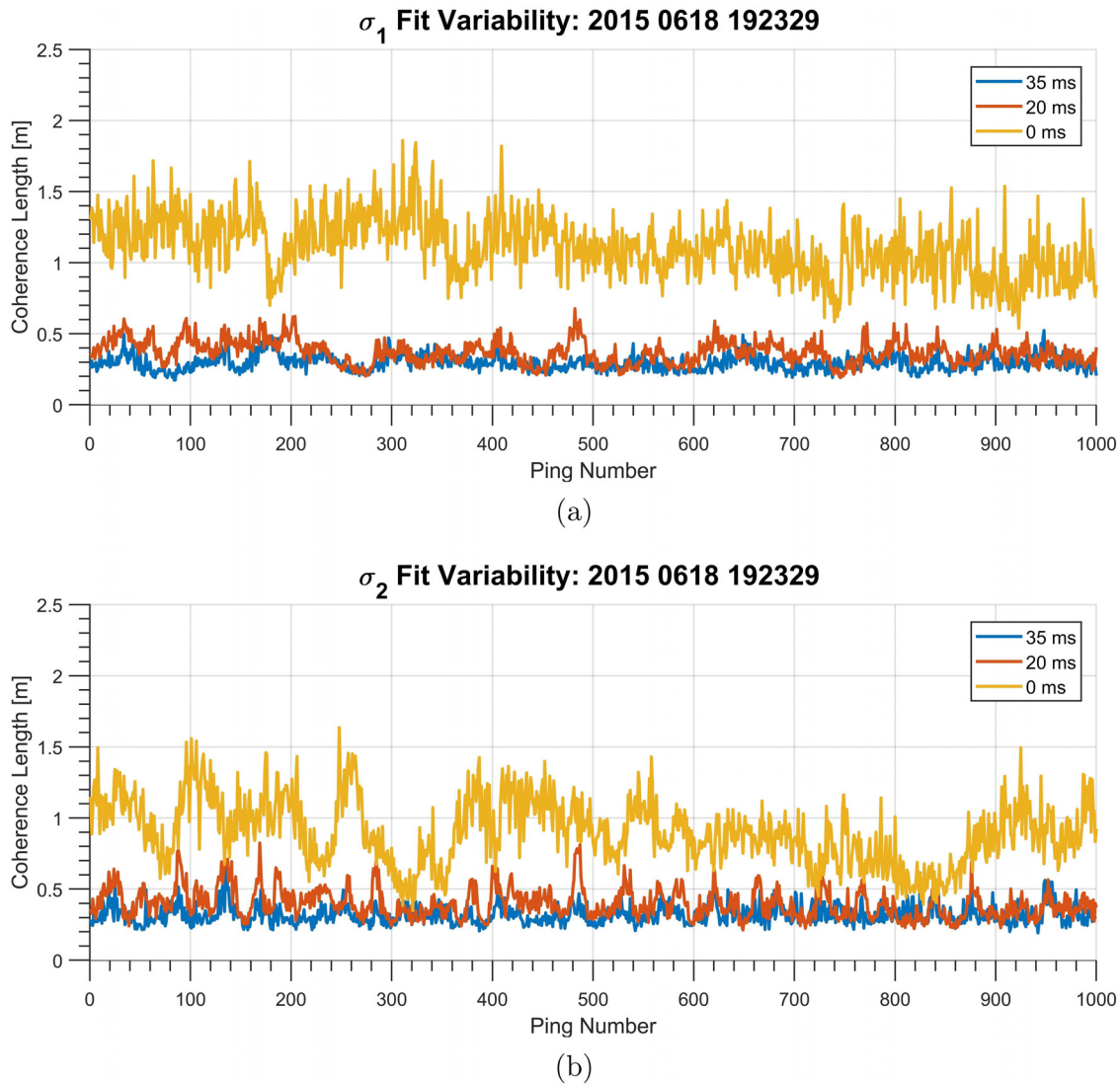


FIG. 13. (Color online) The bivariate normal fit has been applied to each of the 1000 pings of track 192 329. The resulting fit parameters for the array aligned coherence lengths,  $\sigma_1$  and  $\sigma_2$ , are shown in (a) and (b), respectively. When comparing the coherence lengths shown here with the sub-bottom profile in Fig. 7, note that the ping number and the along-track position are very nearly equal because the sensor's ping-to-ping advance is approximately one meter.

layering is absent in sequence 2; however, the scattering is spatially anisotropic. Finally, sequence 1 appears to be spatially isotropic. These observations are in line with those made in the test site geologic setting described in Sec. IV.

In Fig. 11, the spatial coherence surface is shown for each of the nine temporal windows applied to ping 155. The shape of the surface is measured using the bivariate normal fit and the fit parameters are provided in the title of each figure. The surface narrows with increasing inner time and the surfaces are moderately asymmetric. The earliest three to four windows span sequence 3, the post-glacial layered sediments. The coherence lengths for these windows are relatively large. The sediment interfaces in this sequence are associated with a fine-grained sediment that typically have low interface roughness, and Brock (1990) has associated low roughness interfaces with broad spatial coherence. Using the van Cittert-Zernike theorem, Brown (2017) has shown that scattering from a low roughness interface produces a field with wide spatial coherence. Additionally, the field scattered from these layers will include both a coherent

component and an incoherent component. Given these two effects, it is unsurprising to see wide spatial coherence for these windows. Sequence 1 and 2 do not have distinct layers and are therefore less likely to have strong coherent components or broad spatial returns from low roughness interfaces. This results in the significantly shorter coherence lengths observed for these later windows.

Figure 12 provides the same analysis applied to ping 408. Interestingly, a significant change in the asymmetry observed for each window. Figures 12(a)–12(c) show asymmetry oriented where  $\theta_a > 0$ . The orientation abruptly changes to  $\theta_a < 0$  for inner times 15 ms and greater. This change occurs as the temporal window passes from sequence 3 to sequence 2. The orientation and degree of asymmetry for this ping are somewhat constant for Figs. 12(e)–12(i) spanning inner times of 20–40 ms. Remember that a 10 ms temporal window was used in the analysis of this data. Therefore, the windows with inner times of 20 ms, 30 ms, and 40 ms have no temporal overlap and are therefore statistically independent. The consistency of spatial coherence

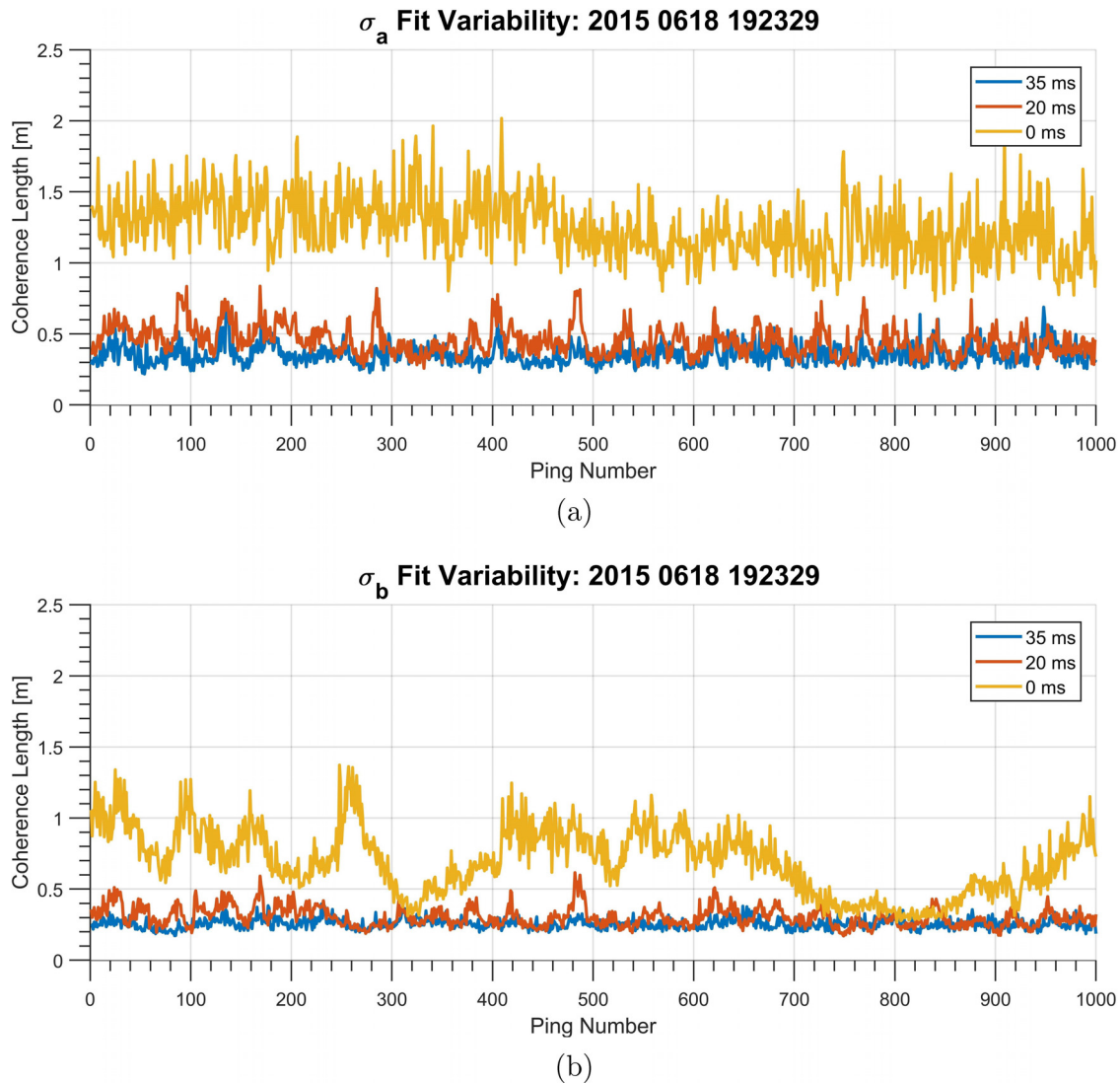


FIG. 14. (Color online) The bivariate normal fit has been applied to each of the 1000 pings of track 192329. The resulting fit parameters for the surface aligned coherence lengths,  $\sigma_a$  and  $\sigma_b$ , are shown in (a) and (b), respectively. When comparing the coherence lengths shown here with the sub-bottom profile in Fig. 7, note that the ping number and the along-track position are very nearly equal because the sensor's ping-to-ping advance is approximately one meter.

over this range indicates that the asymmetry is not due to a random fluctuation of the measured field but instead may be due to an environmental process that is spatially stationary over this range of sediment depths.

To assess the ping-to-ping variability of the measured spatial coherence, the coherence lengths are calculated for every ping of track 192329. The array aligned coherence lengths,  $\sigma_1$  and  $\sigma_2$ , are shown in Figs. 13(a) and 13(b), respectively. The surface aligned coherence lengths,  $\sigma_a$  and  $\sigma_b$ , are shown in Figs. 14(a) and 14(b), respectively. Once again, in each of these figures the coherence lengths for three inner times are selected to represent data from within sequence 1 (35 ms), sequence 2 (20 ms), and sequence 3 (0 ms).

Several interesting observations may be made in comparing the major and minor axis coherence lengths in Fig. 14. First, the coherence lengths observed for the 0 ms temporal window differs significantly from the other two windows. The major axis length for 0 ms fluctuates somewhat randomly around a mean value that slowly decreases over the

1000 ping interval. The minor axis length for the 0 ms window shows more spatial structure from ping-to-ping. Over the first 400 pings,  $\sigma_b$  gradually oscillates between 0.3 meters and 1.4 meters. From ping 600–1000,  $\sigma_b$  begins at 0.9 meters, decreases to near 0.3 meters, and then rises back to 1.0 meters. This interval coincides with the interval of the 1.4 degree maximum slope seen in the sub-bottom profile of the track, Fig. 7. The gradual spatial variation is not indicative of statistical variations in estimation of the coherence length, which would be random from ping-to-ping. Instead, this spatial structure is likely due to the combination of coherent and incoherent scattering from the interfaces and the volumes present in the sequence 3 sediments.

The major axis and minor axis coherence lengths for the 20 ms and 35 ms temporal windows are almost always shorter than that measured for the 0 ms window. Also, neither of these windows show the level of ping-to-ping variability seen in the sequence 3 sediments. For the 20 ms window,  $\sigma_a$  shows some smaller scale (order 10 ping) ping-to-ping spatial variability where the coherence length



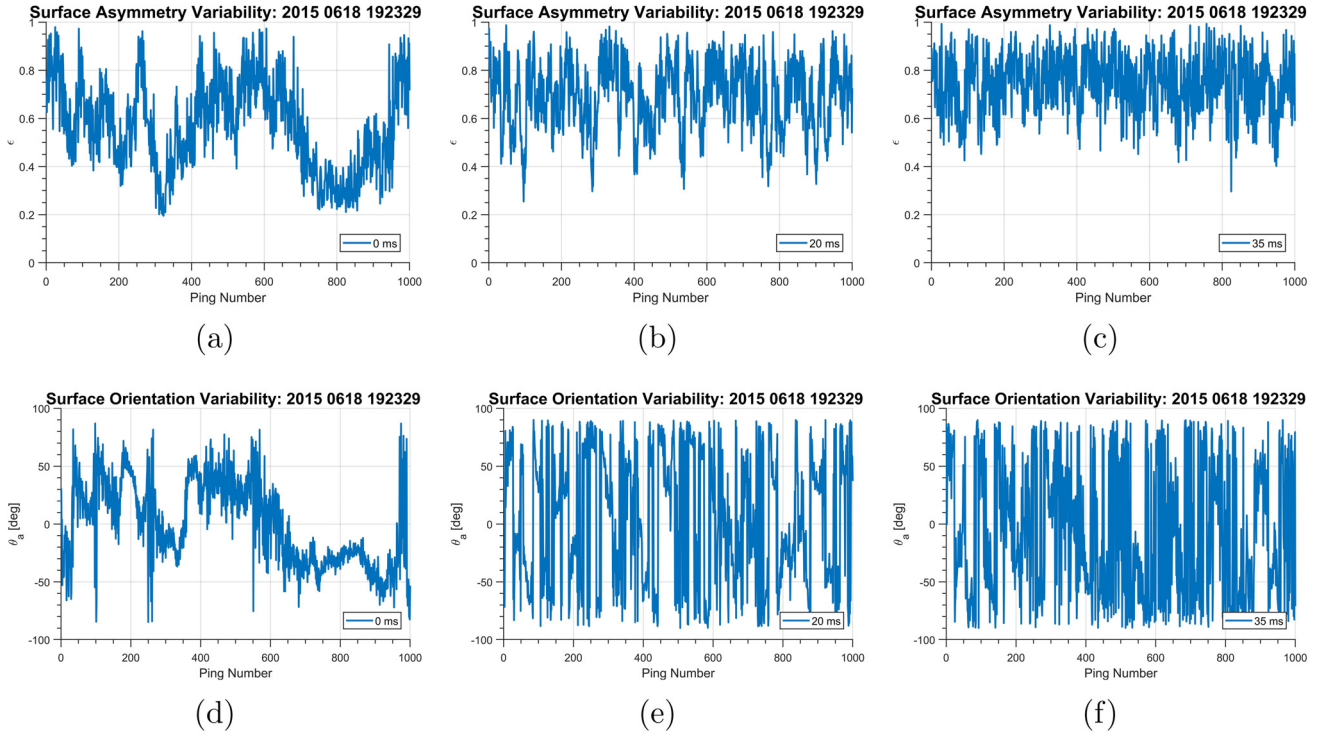


FIG. 15. (Color online) The surface asymmetry parameters  $\epsilon$  and  $\theta_a$  are shown for three selected temporal windows applied to track 192329.  $\epsilon$  is shown in the upper row of figures and  $\theta_a$  in the lower row. The leftmost column includes the figure pair for the 0 ms window, the middle column includes the figure pair for the 20 ms window, and the rightmost column shows the figure pair for the 35 ms window. Note that the ping-to-ping structure of the spatial coherence is strongly dependent on the inner time of the temporal window.

increases above what appears to be a consistent lower bound. For this same temporal window,  $\sigma_b$  shows less ping-to-ping structure. This is the opposite of what was observed for the 0 ms window, where the primary spatial structure was seen in  $\sigma_b$ . Finally, the ping-to-ping spatial structure is a minimum for the 35 ms window. This qualitatively agrees with the observation of isotropic scattering strength in the sub-bottom profiles for this sequence.

The nature of the ping-to-ping structure of the spatial coherence is apparent in Fig. 15. Here, the surface asymmetry,  $\epsilon = \sigma_b/\sigma_a$ , is shown in the upper row of figures and the

orientation,  $\theta_a$ , shown in the lower row of figures. The leftmost column includes the figure pair for the 0 ms window, the middle column includes the figure pair for the 20 ms window, and the rightmost column shows the figure pair for the 35 ms window. The ping-to-ping spatial structure for the sequence 3 asymmetry is apparent in Fig. 15(a). Through the first 400 pings the asymmetry varies from  $\epsilon = 0.2$  to  $\epsilon \sim 1.0$ , and over pings 600–1000 the asymmetry slowly declines from  $\epsilon = 0.9$  to  $\epsilon = 0.2$  before rising back to  $\epsilon = 0.95$ . A visual comparison of the surface asymmetry and its associated orientation [Figs. 15(a) and 15(d)] show that these two properties are correlated.

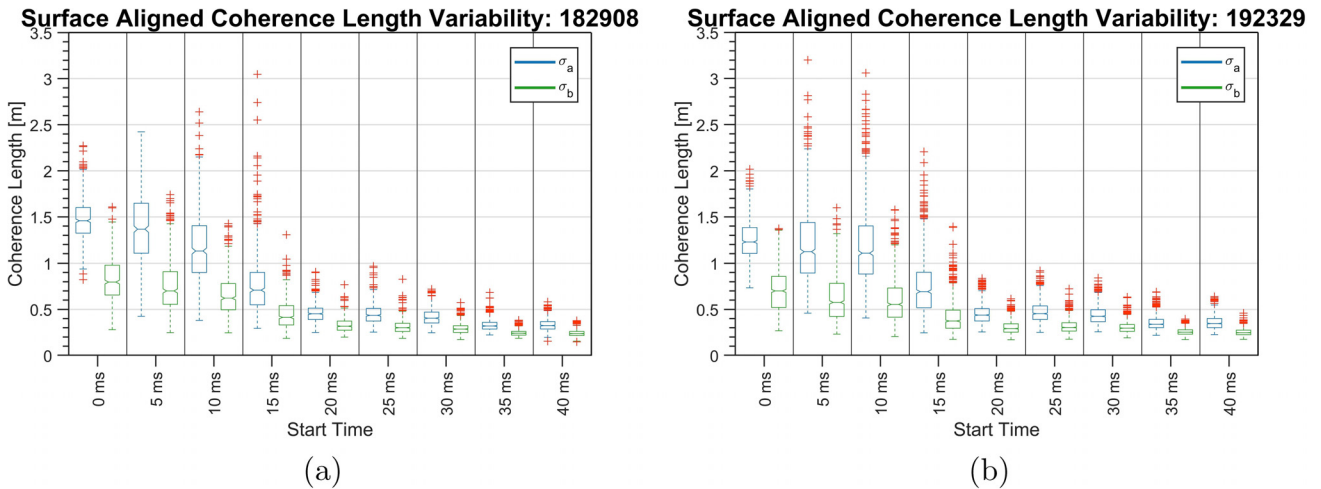


FIG. 16. (Color online) The array aligned coherence lengths,  $\sigma_a$  and  $\sigma_b$ , are shown as a function of the temporal window inner time for track 182908 in (a) and track 192329 in (b). The data are presented using a box-and-whisker plot where the horizontal band in the box indicates the median. The box covers the second and third quartile and the whiskers are 1.5 times the inner quartile range. Points outside the whisker limits are shown individually.

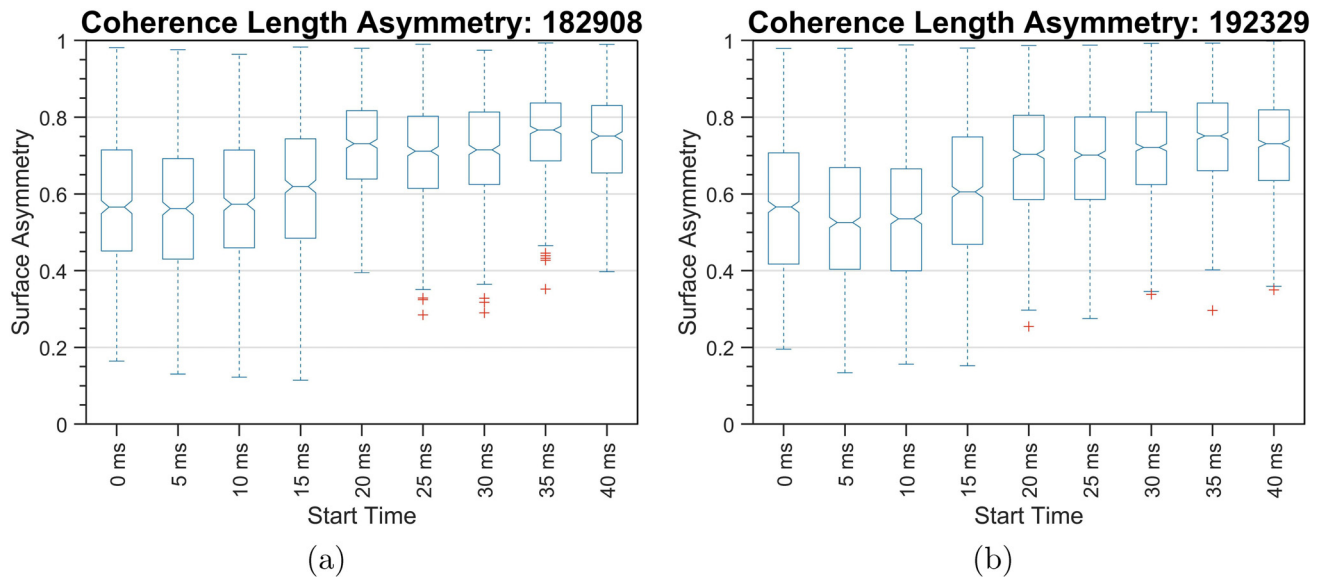


FIG. 17. (Color online) The coherence length asymmetry,  $\varepsilon = \sigma_b/\sigma_a$ , is shown in box and whisker plot as a function of the temporal window inner time for track 182 908 in (a) and track 192 329 in (b).

This is especially true in the 700–900 ping interval where the orientation is nearly constant. The asymmetry and orientation for the 20 ms window also shows ping-to-ping spatial structure; however, the spatial fluctuations occur over shorter ping intervals. The surface orientation for this window is nearly random. Finally, the 35 ms window exhibits random ping-to-ping fluctuations in both the orientation and asymmetry of the spatial coherence surface.

In Fig. 16, the measured, array-aligned coherence lengths are summarized as a function of window inner time for track 182 908 and 192 329. For each inner time, the coherence lengths are shown using a box and whisker plot. In these figures, the blue box corresponds to the major-axis coherence length,  $\sigma_a$ , and the green box corresponds to the minor-axis coherence length,  $\sigma_b$ . The median coherence length is given by the horizontal dividing line within the box. The vertical extent of the box spans the second and third quartile of the measured coherence lengths. The whiskers extend above and below the box by 1.5 times this interquartile (central 50%) range. Any measurements outside the whisker are shown with individual markers.

In Fig. 17, the measured surface asymmetry is summarized as a function of window inner time for track 182 908 and 192 329. Again, the impact of the sequence 3 sediments is apparent in the data. The median surface asymmetry is less than 0.6 for the temporal windows corresponding to the sequence 3 sediments. The spatial coherence of sequence 2 and sequence 1 each show reduced asymmetry as well as a reduced variance of the asymmetry.

Some general observations may be made across the data presented in Figs. 9–17. The 0 ms window has the broadest coherence lengths as well as the most asymmetry between coherence lengths. The asymmetry in this window varies somewhat slowly from ping-to-ping. This indicates that the measured spatial coherence asymmetry is determined in part by environmental effects that are persistent across sequential pings. The 20 ms window has a significantly shorter coherence length than the

0 ms window, and the surfaces generated for this window are less asymmetric. While ping-to-ping spatial structure exists for this window's asymmetry, it is present only over intervals of 10–20 pings. It is hypothesized that the moderate spatial anisotropy of the sequence 2 sediments, seen in Fig. 8, has led to ping-to-ping coherence length variability in the 20 ms window. The spatial coherence length for the 35 ms window is slightly narrower than that observed for the 20 ms window. The surface asymmetry for this window varies randomly from ping-to-ping and the orientation of the surface is random as well.

## VI. CONCLUSION

A multichannel sonar system was used to measure the near-normal incidence scattered field in Seneca Lake, NY. Analysis of this sonar data showed scattering present from both the sediment-water interface and the lakebed sub-bottom. Sub-bottom profiles showed that the lakebed consists of three distinct sediment sequences in the upper 30 meters. Two linear tracks of data that were collected in the central part of the lake were analyzed in detail. For each ping within a track, the spatial coherence was measured by calculating the correlation coefficient among all of the array's possible channel pairs. These measured correlation coefficients were then grouped by spatial offset to form a two-dimensional measure of the spatial coherence surface. This surface is quantitatively characterized through application of a metric based on a bivariate normal fit. This metric provides measures of the coherence length, the length asymmetry, and the asymmetry orientation.

In Sec. V, the ping-to-ping spatial coherence lengths were shown to have significant variability. Through the application of temporal windowing, the coherence variability was characterized as a function of sediment sequence. The observed variability appears to be linked to the complexity and anisotropy of the associated lake floor sub-bottom sequences. In the upper, post-glacial sequence 3 sediments, the discrete sediment layers form smooth interfaces. The

presence of these scattering interfaces will contribute both a coherent and an incoherent component to the scattered field. Small tilts in the orientation of the sub-bottom structure could produce a coherent plane-wave whose direction is not normal to the receive array. This potential directionality of a coherent source will strongly affect the measured coherence. Additionally, the variability could be due to a number of processes that impact the coherent and incoherent components of the scattered field. Small scale curvature of the strata that match the wavefront curvature of the incident sound field can have a focusing effect. Harrison (1971) has observed this effect in radio scattering from the Antarctic Ice Sheet and Claerbout (1985) has attributed this effect to enhanced scattering levels in geophysical surveys. Additionally, discrete scattering objects may be present in the lake bed. This could be due to small collections of natural inhomogeneous material. The uppermost sequence, which is spatially anisotropic and includes significant layering, exhibited the highest variance in the measured coherence lengths and eccentricity. Scattering from the deeper sediment sequences is more spatially isotropic and the resulting coherence lengths show reduced variability.

## ACKNOWLEDGMENTS

The authors would like to thank Zackary Lowe for his role in the developing of the sonar test platform and operating the sonar system during the experiment. The authors would like to thank Charles Holland for applying the Bryan method that produced the sediment sound speed estimates described in Sec. IV. This research was supported by the United States Office of Naval Research.

- Belletini, A., and Pinto, M. A. (2002). "Theoretical accuracy of synthetic aperture sonar microneavigation using a displaced phase centre antenna," *IEEE J. Oceanic Eng.* **27**(4), 780–789.
- Berkson, J., Dicus, R., Field, R., Morris, G., and Anderson, R. (1980). "Measurements of spatial coherence of bottom-interacting sound in the Tagus Abyssal Plain," in *Bottom-Interacting Ocean Acoustics*, edited by W. A. Kuperman and F. B. Jensen, Vol. 5 of NATO Conference Series (Springer, New York), pp. 623–641.
- Berkson, J. M. (1980). "Measurements of coherence of sound reflected from ocean sediments," *J. Acoust. Soc. Am.* **68**(5), 1436–1441.
- Boltryk, P. J., Hill, M., Keary, A. C., and White, P. R. (2004). "Surface fitting for improving the resolution of peak estimation on a sparsely sampled two-dimensional surface with high levels of variance, for an acoustic velocity log," *Meas. Sci. Technol.* **15**(3), 581–591.
- Born, M., and Wolf, E. (1999). *Principles of Optics*, 7th ed. (Cambridge University Press, New York), p. 554.
- Brock, E. M. (1990). "Error analysis of correlation logs," in *Proceedings of the IEE Colloquium on Inertial Navigation Sensor Development*, January 9, London, UK, pp. 6/1–6/7.
- Brown, D. C. (2017). "Modeling and measurement of spatial coherence for normal incidence seafloor scattering," Ph.D. thesis, The Pennsylvania State University, College Station, PA.
- Brown, D. C., Brownstead, C. F., Gabrielson, T. B., and Lyons, A. P. (2017). "A metric for characterization of two-dimensional spatial coherence," *J. Acoust. Soc. Am.* **142**(3), EL313–EL318.
- Bryan, G. M. (1980). "The hydrophone-pinger experiment," *J. Acoust. Soc. Am.* **68**(5), 1403–1408.
- Carey, W. M. (1998). "The determination of signal coherence length based on signal coherence and gain measurements in deep and shallow water," *J. Acoust. Soc. Am.* **104**(2), 831–837.
- Claerbout, J. F. (1985). *Imaging the Earth's Interior* (Blackwell Science Inc., New York), pp. 7–8.
- Clay, C. S. (1966). "Coherent reflection of sound from the ocean bottom," *J. Geophys. Res.* **71**(8), 2037–2046, <https://doi.org/10.1029/JZ071i008p02037>.
- Coates, D. R. (1968). "Finger lakes," in *Geomorphology, Encyclopedia of Earth Science* (Springer Berlin-Heidelberg), pp. 351–357.
- Curtin, T. M., Morgan, C. K., Petrick, B., Lyons, D., Crocker, M., Rogers, C. E., and Baker, A. P. (2008). "Reconstructing periods of enhanced precipitation during the late glacial and holocene in the Finger Lakes Region, NY," *Northeast. Geol. Environ. Sci.* **30**(4), 277–288.
- Dickey, F. R., and Edward, J. A. (1978). "Velocity measurement using correlation sonar," in *Proceedings IEEE Position Location and Navigation Symposium*, November 6–9, San Diego, CA, pp. 255–264.
- Eckart, C. (1953). "The scattering of sound from the sea surface," *J. Acoust. Soc. Am.* **25**(3), 566–570.
- Frazier, M. E. (1974). "Study of the properties of the outputs of a multielement sonar receiving array operating in a reverberant environment," Ph.D. thesis, The University of Texas at Austin, Austin, TX.
- Guillon, L., Holland, C., and Barber, C. (2011). "Cross-spectral analysis of midfrequency acoustic waves reflected by the seafloor," *IEEE J. Ocean. Eng.* **36**(2), 248–258.
- Halfman, J. D. (2011). "Water quality of Seneca Lake, New York: A 2011 update," Technical Report Finger Lakes Institute of Hobart and William Smith Colleges.
- Halfman, J. D., and Herrick, D. T. (1998). "Mass movement and reworking of late glacial and postglacial sediments in northern Seneca Lake, New York," *Northeast. Geol. Environ. Sci.* **20**, 227–241.
- Harris, F. (1978). "On the use of windows for harmonic analysis with the discrete Fourier transform," *Proc. IEEE* **66**(1), 51–83.
- Harrison, C. H. (1971). "Radio-echo sounding: Focusing effects in wavy strata," *Geophys. J. Int.* **24**(4), 383–400.
- Jackson, D. R., and Moravan, K. Y. (1984). "Horizontal spatial coherence of ocean reverberation," *J. Acoust. Soc. Am.* **75**(2), 428–436.
- Ludlam, S. D. (1967). "Sedimentation in Cayuga Lake, New York," *Limnol. Oceanogr.* **12**(4), 618–632.
- Lynch, J. F., Duda, T. F., Siegmann, W. L., Holmes, J., and Newhall, A. E. (2013). "The Carey Number in shallow water acoustics," in *Proceedings of the 1st International Conference and Exhibition on Underwater Acoustics*, June 23–28, Corfu, Greece, pp. 1149–1160.
- Lyons, A. P., and Weber, T. C. (2007). "A multibeam sonar survey for benthic lake habitat: Assessing the impact of invasive mussels in Seneca Lake, New York," in *Proceedings of the International Conference on Underwater Acoustic Measurements*, June 25–29, Heraklion, Crete, Greece, pp. 871–876.
- Mullins, H. T., and Hinchey, E. J. (1989). "Erosion and infill of New York Finger Lakes: Implications for Laurentide ice sheet deglaciation," *Geology* **17**(7), 622–625.
- Mullins, H. T., Hinchey, E. J., Wellner, R. W., Stephens, D. B., Anderson, W. T., Dwyer, T. R., and Hine, A. C. (1996). "Seismic stratigraphy of the Finger Lakes: A continental record of Heinrich event H-1 and Laurentide ice sheet instability," *Geol. Soc. Am. Special Papers* **311**, 1–35.
- Schock, S., Tellier, A., Wulf, J., Sara, J., and Ericksen, M. (2001). "Buried object scanning sonar," *IEEE J. Ocean. Eng.* **26**(4), 677–689.
- Smith, B. V., and Atkins, P. R. (1991). "Horizontal spatial correlation of bottom reverberation for normal incidence," *J. Acoust. Soc. Am.* **89**(5), 2197–2206.
- Stewart, A., and Ord, J. K. (1994). *Kendall's Advanced Theory of Statistics* (Halsted Press, New York), Vol. 1, p. 565.
- Tang, D., and Frisk, G. V. (1995). "Spatial correlation of acoustic waves scattered from a random ocean bottom," *J. Acoust. Soc. Am.* **97**(5), 2783–2803.
- Urick, R. J., and Lund, G. R. (1964). "Vertical coherence of explosive reverberation," *J. Acoust. Soc. Am.* **36**(11), 2164–2170.
- Weber, T. C., and Lyons, A. P. (2006). "A multibeam survey of mid-Seneca Lake: Bathymetry, backscatter, and invasive species," in *Proceedings of the (FLRC)*, November 17, Geneva, NY, p. 380.
- Wilson, G. R. (1982). "Comparison of the measured covariance of surface reverberation for horizontal and vertical arrays," *J. Acoust. Soc. Am.* **72**(6), 1905–1910.
- Wilson, G. R., and Frazier, M. E. (1983). "Horizontal covariance of surface reverberation: Comparison of a point scatterer model to experiment," *J. Acoust. Soc. Am.* **73**(3), 749–760.